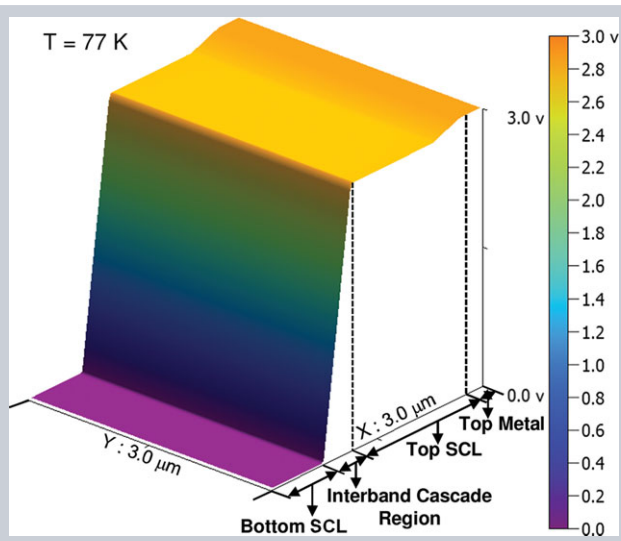


LASER & PHOTONICS REVIEWS

Abstract Dynamic charge carriers play a vital role in active photonic quantum/nanodevices, such as electrically pumped semiconductor lasers. Here we present a systematic experimental study of gain-providing charge-carrier distribution in a lasing interband cascade laser. The unique charge-carrier distribution profile in the quantum-well active region is quantitatively measured at nanometer scales by using a noninvasive scanning voltage microscopy technique. Experimental results clearly confirm the accumulation and spatial segregation of holes and electrons in the beating heart of the device. The measurement also shows that the charge-carrier density is essentially clamped in the presence of stimulated emission at low temperatures. The threshold charge-carrier density exhibits a linear but fairly weak temperature dependence, in contrast to the exponential temperature dependence of the threshold current. The experimental approach will lead to a deeper understanding of fundamental processes that govern the operation and performance of nanoelectronic devices, quantum devices and optoelectronic devices.



Nanoscopically resolved dynamic charge-carrier distribution in operating interband cascade lasers

Rudra S. Dhar¹, Lu Li², Hao Ye², Seyed G. Razavipour¹, Xueren Wang¹, Rui Q. Yang², and Dayan Ban^{1,*}

1. Introduction

Electrically pumped semiconductor lasers have been employed for many ubiquitous applications such as telecommunication, gas sensing, and optical disc drivers, to name just a few [1–6]. For designing and fabricating high-performance semiconductor lasers, optical gain-providing charge carriers need to be efficiently injected into the desired energy states in the active region, from which photons are generated and light is emanated [7, 8]. The semiconductor lasers can be categorized into two groups based on the types of charge carriers involved: bipolar lasers, in which both electrons and holes are injected into the active region for radiative recombination [9, 10]; and unipolar lasers, in which only one type of carrier (typically electrons) is flowing throughout the active region for light generation [11]. Interband cascade lasers (ICLs) [12, 13] that exploit the cascading mechanism for achieving high voltage efficiency and quantum efficiency are actually bipolar devices in which equal numbers of electrons and holes are generated from an internal semimetallic interface, with electron injection in one direction and hole injection in the opposite direction [14, 15]. The advantages of an ICL over a conventional diode laser include uniform injection of carriers to each

active region module, which is ensured by the series connection in the structure, and lower carrier concentration for lasing threshold [16]. As such, ICLs have become one important coherent light source that covers a wide range of the midinfrared wavelength spectrum [14–20] with continuous-wave operation at room temperature (e.g., 3–6 μm) [21–23].

Regardless of the different operating principles in these lasers, charge-carrier distribution inside the MQW active region plays a critical role in governing device functionality and performance. Though intensive theoretical models have been developed to calculate the charge-carrier distribution profile in semiconductor quantum structures [24–28], the simulation results have rarely been verified in a direct manner due to lack of counterpart data from experiments. The nanoscopic reasons for many failures and degradation of device operation remain puzzling as a result. For example, modeling suggests that a single hole-injector quantum well (QW) would suffice in an ICL, nevertheless, empirical studies have found improvement when the second GaSb QW is included to make the tunneling barrier quite thick [15]. Recently, record-breaking device-performance improvement of ICLs was reported and was attributed to rebalancing of electrons and holes in the active region, but only through nanoscopically

¹ Department of Electrical & Computer Engineering, Waterloo Institute for Nanotechnology, University of Waterloo, 200 University Ave W., Waterloo, ON, N2L 3G1, Canada

² School of Electrical & Computer Engineering, University of Oklahoma, Norman, Oklahoma, 73019, USA

*Corresponding author: e-mail: dban@uwaterloo.ca

modeling carrier density profile and macroscopically measuring device input/output behaviors [21]. Apparently, quantitative and direct measurements of inner workings such as charge-carrier density profile would greatly facilitate in-depth understanding of the underlying physics in ICLs, leading to technology advancement and innovation.

In what follows, we present the detailed experimental measurement of the internal charge-carrier density profile of an actively biased interband cascade laser from 77 K up to room temperature by using scanning voltage microscopy technology. We reveal that electrons and holes segregate spatially in the undoped multiple quantum-well active region, and nevertheless, remain overall balanced in total charges, directly confirming the hypothesis of rebalancing of electrons and holes by heavily n-doping the electron-injection layers [21]. The experimental results unambiguously show that the charge-carrier density in the MQW active region is essentially clamped in the presence of stimulated emission at low temperatures while monotonically increasing with device bias otherwise. In contrast to the exponential temperature dependence of the threshold current, the clamped charge-carrier density of the ICL sample is found to slowly increase with temperature from 77 K to its maximum lasing temperature (~ 248 K), indicating a fairly weak temperature dependence of the threshold gain.

2. Experiments

A commercial cryogenic-temperature atomic force microscope (AFM) is employed to set up the scanning voltage microscopy (SVM) measurements [29–31]. The sample under test is mounted on a sample holder (heat sink) inside the AFM microscope head. The device (heat-sink) temperature is monitored and kept at 77 K during the SVM scans by submerging the AFM microscope head into a chamber full of liquid nitrogen or at higher temperatures by retreating the sample from the liquid nitrogen chamber. A conductive AFM probe (diamond-coated, boron-doped Si cantilever probe, spring constant 40 N/m, radius of probe tip ~ 20 nm) is scanned in contact mode over the transverse cross section of the device to access the voltage signal (see Supporting Information Fig. S1). The ICL sample under test (R090) consists of eight periods of active and injection sections with a peak emission wavelength of ~ 4.3 μm at 77 K. Each period of the active section (where radiative recombination occurs) has two InAs electron quantum wells and two GaInSb hole quantum wells [17]. The electron injection section is made of InAs/AlSb(As) digitally graded quantum wells. The eight cascade modules are sandwiched by the top and bottom micrometer-thick undoped InAs separate confinement layers (see Supporting Information Fig. S3). Some quantum wells in the electron injection region are n-doped to 4.3×10^{18} cm^{-3} , in order to achieve rebalancing of electrons and holes in the active section of the device [21]. The laser structure (R090) was grown using a molecular beam epitaxy (MBE) system on a n^+ -doped InAs substrate and then a piece of the wafer was processed into a narrow-

ridge (10 μm wide and 1 mm long) waveguide laser with both facets uncoated. The ICL device is externally biased in pulsed mode to avoid potential overheating problems by using an AVTech pulse generator. This laser wafer was designed for examining electrical tuning [17] rather than for achieving high-temperature operation. Hence, the maximum lasing temperature of the ICL device used in this paper is 248 K (at which the threshold voltage is 3.8 V).

3. Results and discussion

Figure 1a illustrates a two-dimensional voltage profile across the device active region that is obtained by scanning a conductive cantilever probe over a transverse cross-sectional area (3×3 μm^2) on the front emission facet. The measured voltage drops monotonically from the top metals (positively biased at 3 V), across the intermediate layers, to the grounded bottom SCL/contact layers (at 0 V). Four sections are clearly resolved due to their contrast in electric potential – the top metal layer, the top SCL layer (undoped InAs), the interband cascade region layer (eight cascade modules) and part of the bottom SCL/contact layer. As expected, most of the voltage drop occurs over the 386-nm thick interband cascade region of the device. The topology image obtained simultaneously from the atomic force microscopy scans confirms that the cross section of the front emission facet is almost atomically flat.

Similar SVM scans are performed at different applied device biases from 0.5 V up to 5.0 V with a step of 0.5 V at 77 K. By averaging cross-sectional line scans that make up a two-dimensional (2D) SVM image similar to the one shown in Fig. 1a, one-dimensional SVM measured voltage profile curves are obtained as a function of the distance from the top metal layer (Fig. 1b). The slope of the voltage profile curve is almost uniform over the interband cascade region (thus indicating a constant electric field) and increases proportionally with the increase of the applied bias on the device. Zoomed-in scans disclose that the electric field in the interband cascade region is actually not always constant, which will be discussed in detail shortly. A slight voltage drop is observable at the top contact layer/top SCL layer interface, which is likely attributed to the reverse-biased junction between the n^+ InAs contact layer (n -doped $\sim 1 \times 10^{19}$ cm^{-3}) and the nominally undoped InAs SCL (which might have background n -type doping $\sim 1 \times 10^{16}$ cm^{-3}) near the interface. This undesired voltage drop is only 0.13 V at a device bias of 5 V, confirming the high voltage efficiency ($(5 - 0.13)/5 \times 100\% = 97.4\%$) in the ICL devices.

Individual cascade modules can be resolved in high-resolution SVM scans by reducing the scan range. Figure 2a shows such a two-dimensional voltage profile over a smaller area of 512×512 nm^2 . It is revealed that every ~ 48 nm in distance a pair of voltage dips can be observed, denoted by dashed lines. There are in total eight such pairs over the interband cascade region, corresponding to the eight cascade modules in the device. The measured 48 nm period agrees well with the design module thickness (386 nm/8

= 48.25 nm). Such voltage dips are measured at all device biases from zero bias to 5 V, while the magnitude of the voltage dip depends on the applied device bias and is in the range of microvolts up to a few mV (see Supporting Information Fig. S2). The internal electric field (F) inside the MQW active region can be obtained by calculating the first-order derivative of voltage against distance ($F = -dV/dx$), as plotted in Fig. 2b, clearly delineating the exact location of the voltage dips. At a device bias of 3.5 V, the average electric field across the MQW active region is $F = 8.64 \text{ V}/\mu\text{m}$ (86.4 kV/cm). Over each of the eight voltage

dip pair regions the electric field oscillates dramatically, yielding two peaks and two valleys. As will be discussed in more detail shortly, the nonuniform electric field is a direct indicator of the expected spatial segregation of electrons and holes in the unique type-II quantum wells in the active sections of this ICL device.

The voltage dip pairs become more perceivable by further zooming in on the voltage profile curve. As shown in Fig. 2c, each voltage dip pair spans a distance of $\sim 9 \text{ nm}$ and the magnitude of the voltage dips is around 7 mV at the device bias of 3.5 V. The first voltage dip pairs are located $\sim 5 \text{ nm}$ away from the interface of the undoped InAs top SCL layer and the interband cascade region, corresponding to the nominal coordinates of the InAs/GaInSb MQW active section of the first cascade module (see Fig. 2d). Since the rest voltage dip pairs repeat every $\sim 48 \text{ nm}$, they therefore coincide with the InAs/GaInSb MQW active section of the corresponding modules, respectively. Figure 2c also shows more detailed features of the electric-field distribution profile, which are almost identical in each of the eight cascade modules (the figure only shows the first two modules). The identical electric-field distribution profile among the eight cascade modules represents uniform carrier injection and distribution in each of the modules, ensured by the aforementioned series connection in the structure [14, 15]. Perhaps more strikingly, from the voltage-distribution profile, one can derive the net charge-carrier density profile ($n(x)$) by calculating the second order-derivative of $V(x)$ as

$$n(x) = -\frac{\epsilon_0 \epsilon_r}{q} \frac{d^2 V(x)}{dx^2}, \quad (1)$$

where ϵ_0 is the vacuum permittivity, ϵ_r the relative permittivity and q the electron charge. The calculated $-d^2 V/dx^2$ results are plotted in Fig. 2d, together with the band diagram of the active and injection sections at zero bias. The second-order derivative curve ($-d^2 V/dx^2$) appears somewhat zigzagged due to the limited spatial resolution in our SVM scans (scan step: 1 nm). Nevertheless, it shows that the net charge density is zero in the hole injector and most of the electron-injector section, while negative net charges accumulate in the two InAs conduction-band quantum wells of the active section and positive net charges accumulate in the two GaInSb valence-band quantum wells of the active section as well as the first AISb valence-band quantum well of the electron-injector section. Apparently, electrons and holes are injected into the active section for radiative recombination, but they spatially segregate from each other due to the unique band alignments in the type-II antimonide system [14, 15]. Note that this SVM result marks a direct and first-ever observation of charge-carrier distribution while the semiconductor quantum laser is in operation, illustrating the great potential for SVM techniques to advance research and development in ICL and other quantum/nano areas. Theoretical modeling has disclosed substantial electron accumulation in the electron injector quantum wells by heavy n-doping [15]. Such electron-density distribution is,

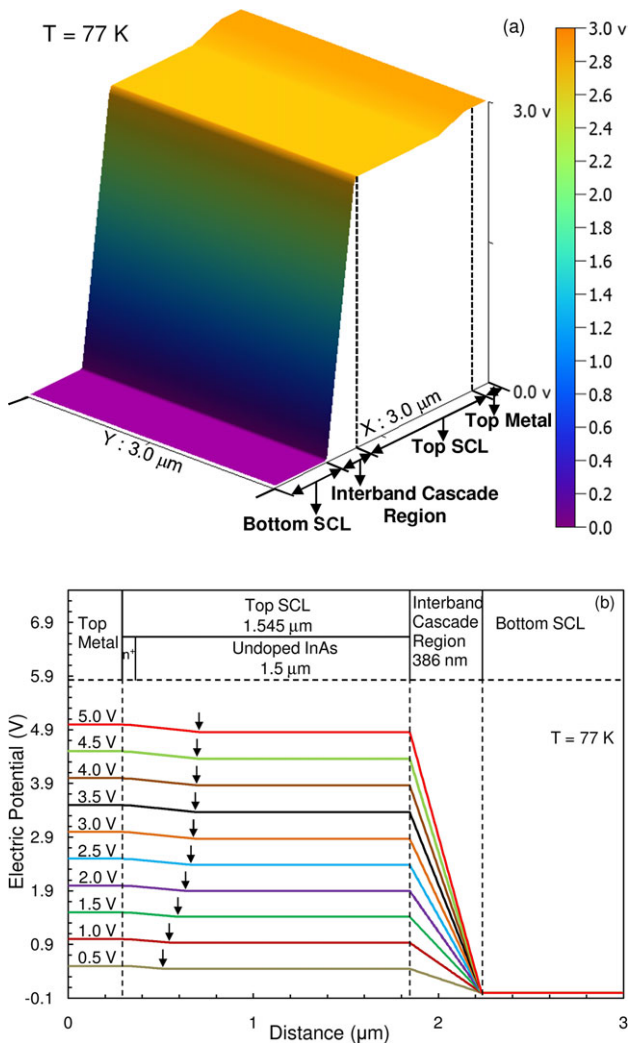
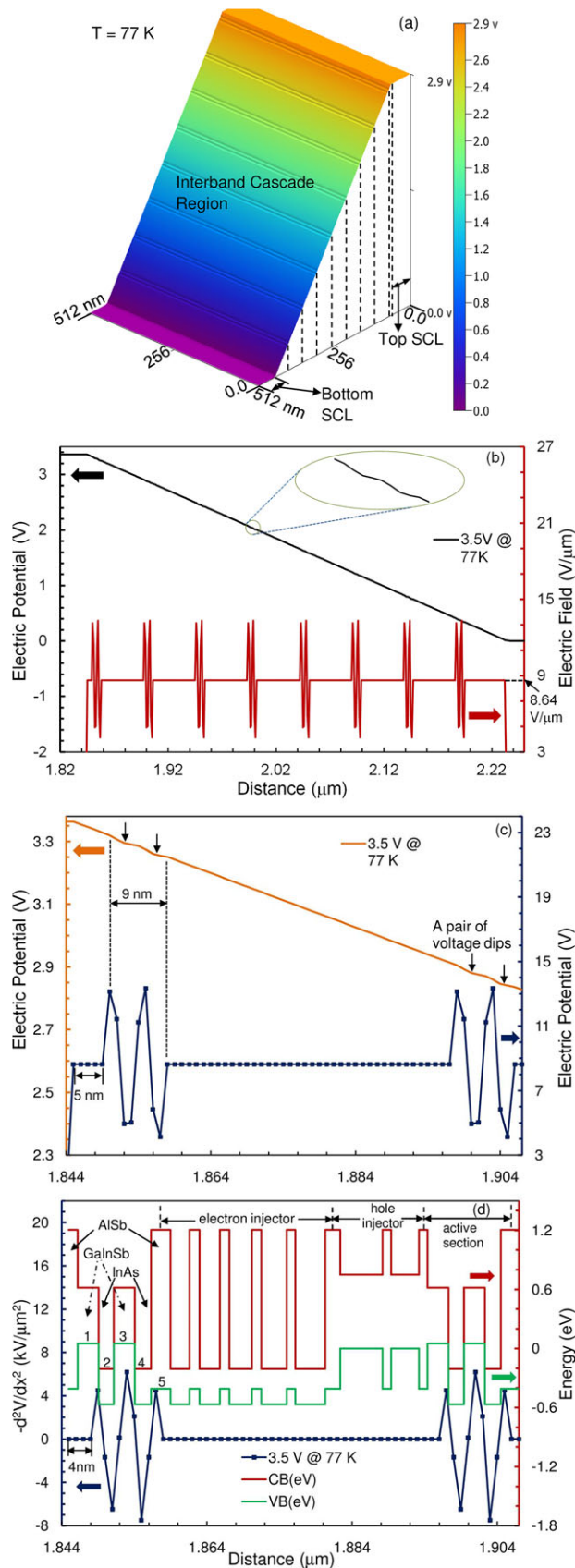


Figure 1 Scanning voltage microscopy across the ICL device. (a) An SVM two-dimensional (2D) voltage profile image for $3 \mu\text{m}$ distance from the top contact to the bottom contact layer at an applied bias of 3.0 V and a cryogenic temperature of 77 K. (b) One-dimensional (1D) section analysis of the SVM voltage profiles at 77 K for biases 0.5–5.0 V in steps of 0.5 V. The SVM scans clearly shows a voltage drop at the junction of the undoped InAs separate confinement layer (SCL) to the n^+ InAs contact layer where a depletion region is formed. The active region is measured to be $\sim 384 \text{ nm}$ thick, which is very close to the design thickness value of the device.



however, not observed in the injector section in our SVM measurements, which might likely be attributed to the negative charges of the accumulated electrons being mostly neutralized by the positive charges of the ionized n-type dopants in the same region, since this SVM technique is only sensitive to net electric charges.

The charge-carrier sheet density in each of the quantum wells of the active section can be calculated by integrating $n(x)$ as

$$\sigma_i = \int_i n(x) dx \quad (2)$$

where σ_i is the charge-carrier sheet density in the i th quantum well of the active section and $n(x)$ is the net charge-carrier density profile obtained earlier. The symbol $i = 1, 2, 3, 4, 5$, corresponds to the first GaInSb hole well, the first InAs electron well, the second GaInSb hole well, the second InAs electron well and the first AlSb hole well in the electron-injector section, respectively, in the order from left to right in Fig. 2d. The experimental charge-carrier sheet densities (σ_i) obtained by performing the integration of Eq. (2) are plotted as a function of the applied device bias at 77 K in Fig. 3a. The carrier sheet density first increases quickly with the device bias, and gradually saturates at higher biases. The dashed line denotes the threshold voltage (3.4 V) of the ICL sample at 77 K. As expected, the carrier density in the active section is essentially clamped when the device starts lasing – all additional injected carriers are consumed by stimulated emission [1]. Similar measurements and calculations are repeated at room temperature for comparison, at which temperature the ICL device does not lase. The experimental sheet charge-carrier densities (σ_i) at room temperature are plotted in Fig. 3b, showing a monotonic increase over the entire device bias range from zero to 4 V. In the absence of stimulated emission, the carrier density in the active section is not clamped when current injection continuously increases. The total hole and electron sheet

Figure 2 Periodic nonuniform electric field across cascade modules. (a) A zoomed-in 2D voltage profile on the interband cascade region portion (512 nm × 512 nm) at 77 K and an applied bias of 3.0 V. The interband cascade region and the undoped InAs SCL are denoted. Eight pairs of voltage dips are clearly observed and denoted with dotted lines at every ~48 nm, representing the eight modules in the interband cascade region. (b) A 1D voltage profile (over a distance of 512 nm) at 77 K and an applied bias of 3.5 V with corresponding electric field ($-dV/dx$) distribution across the region. Eight pairs of periodic spikes in the electric field curve. (c) A zoomed-in voltage profile (over a distance of 63 nm) starting from the top part of the active region portion at 77 K and 3.5 V. Two pairs of voltage dips in the voltage profile together with the corresponding pairs of electric field spikes are resolved with each pair spanning ~9 nm in distance. (d) The zoomed-in profile ($-d^2V/dx^2$) at 3.5 V, numerically derived from the electric field curve in (c), together with a zero-bias band diagram of the multiple quantum wells in the active region of the device. The value ($-d^2V/dx^2$) is a direct indicator of the net charge-carrier distribution in the active region, with peaks representing positive-charge accumulation and valleys representing negative-charge accumulation.

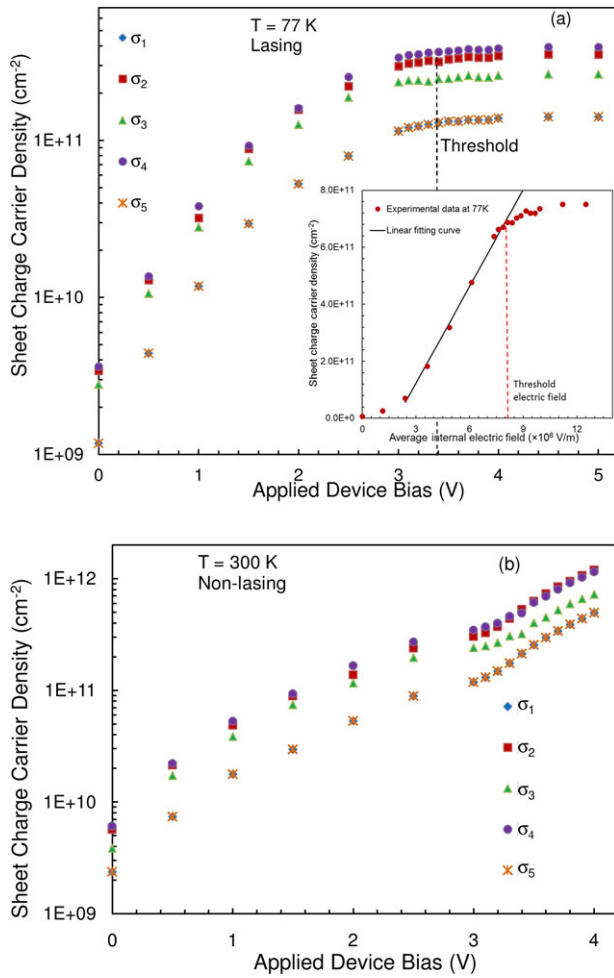


Figure 3 Clamping and nonclamping of charge-carrier density. (a) The experimental sheet charge-carrier densities (σ_i , $i = 1, 2, 3, 4, 5$) as a function of device bias at 77 K, at which temperature the device lases at 3.4 V. (b) The experimental sheet charge-carrier densities (σ_i , $i = 1, 2, 3, 4, 5$) as a function of device bias at room temperature, at which temperature the device does not lase. The inset of (a) shows the experimental total electron density ($\sigma_2 + \sigma_4$) as a function of the internal average electric field. The solid line is a linear fitting curve based on Eq. (3).

densities in the active section are calculated at different biases, confirming the charge neutrality within the experimental uncertainty ($\sim 10\%$) (see Supporting Information Table 1).

A simple model has been developed to estimate the quasiequilibrium charge-carrier sheet density [15]. Assuming equal electron and hole concentration is generated by the overlap (E_{SM}) of the conduction and valence bands at the type II semimetallic interface with parabolic bands, and assuming $E_{SM} \gg k_B T$ and two-dimensional densities of states, the generated charge-carrier sheet densities are given by [15]

$$\sigma_h = \sigma_e \approx m_r^* \frac{E_{SM}}{\pi \hbar^2} \quad (3)$$

where m_r^* is the reduced effective mass, \hbar is the reduced Planck constant and E_{SM} is the overlap energy. E_{SM} depends on electric field (F) as $E_{SM} = qF \times \Delta d - E_i$, where Δd is the center-of-mass distance between the electron and hole wavefunction distributions across the type-II interface. The spatially indirect bandgap (E_i) could vary drastically in growth and is difficult to be precisely calculated from modeling. Equation (3) clearly shows that when the assumption conditions are satisfied, the charge-carrier sheet densities would exhibit an approximately linear dependence on the internal electric field. We note that Δd varies with the electric field, but such a variation is relatively small in type-II heterostructures compared to their already substantial separation at zero bias. We thus set Δd as a constant fitting parameter in our data analysis. In the inset of Fig. 3a the experimental electron sheet density at 77 K is plotted as a function of the average internal electric field, together with a linear fitting based on Eq. (3). Over the electric field range of 2.399×10^6 V/m (23.99 kV/cm) to 8.133×10^6 V/m (81.33 kV/cm) (corresponding to applied device biases from 1.0 V to 3.3 V), the linear fitting curve matches well to experimental data. The fitting yields Δd to be 7.6 nm, somewhat larger as expected than the separation value of 7.4 nm at zero bias from wavefunction calculations. The spatially indirect bandgap (E_i) is derived to be 14.6 meV. Above the threshold electric field the electron sheet density is essentially clamped and thus deviates from the linear fitting curve. For smaller electric fields (below 23.99 kV/cm), Eq. (3) does not apply as there is no energy overlap at the type-II interface.

The SVM technique provides a direct experimental means to investigate the temperature dependence of the threshold carrier sheet density. This ICL device lases up to 248 K (T_{max}), at which the threshold voltage is 3.8 V. A series of SVM scans were therefore performed at a bias of 3.8 V at different temperatures from 77 K to room temperature. For any given temperature lower than T_{max} , the threshold voltage is lower than 3.8 V. Since the charge-carrier sheet density is essentially clamped above the threshold voltage at low temperatures, the carrier density measured at 3.8 V should equal its threshold value at this given temperature. As such, the consistency in comparing the threshold carrier sheet density for all temperatures lower than 248 K is ensured by choosing 3.8 V as the device bias in these series SVM measurements.

Figure 4 presents the measured data of the total electron sheet density (σ_e) and the total hole sheet density (σ_h) in the active section as a function of temperature, showing together is the measured threshold current of the device. The threshold current slowly increases with temperature from 60 K to 170 K, then increases rapidly till T_{max} . In contrast, the threshold charge-carrier density exhibits an almost linear but slow increase with temperature from 77 K to 240 K. At temperatures above T_{max} , the total charge-carrier sheet density is no longer clamped in the absence of stimulated emission and therefore increases rapidly. In particular, the measured carrier density at room temperature is more than twice the value at 240 K. The optical gain in the active section is typically proportional to the population inversion,

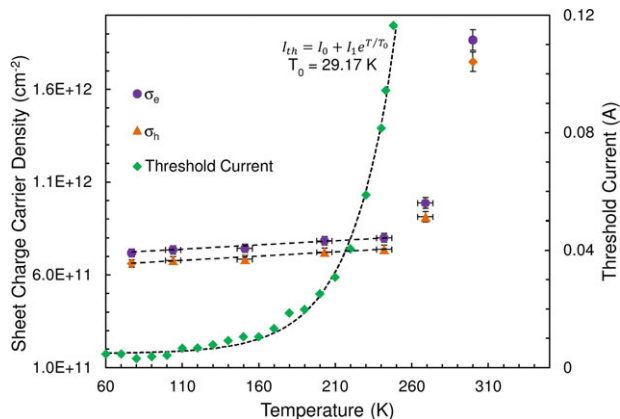


Figure 4 Temperature dependence of charge-carrier density. The active-region charge-carrier sheet densities (σ_h and σ_e) are measured at 3.8 V for different temperatures from 77 K to room temperature. Both increases linearly but slowly with temperature until the maximum lasing temperature (T_{max}). Afterwards, T_{max} , σ_h and σ_e increase rapidly with temperature. The experimental threshold current is also plotted over the same temperature range for comparison, which shows a much stronger temperature dependence.

namely the charge-carrier density. The SVM results thus indicate the optical gain may not change substantially over the temperature range of 77 K to 240 K. Nevertheless, the strong temperature dependence of the threshold current (characteristics temperature $T_0 = \sim 29$ K) may suggest that the carrier lifetime of the lasing states experience fast decrease at temperatures above 170 K. The mechanism for such a fast reduction of carrier lifetime, as pointed out earlier [32], could be attributed to the nonradiative Auger recombination process, which may increase by a factor of 64 when temperature increases from 78 K to 270 K [33].

Much higher T_0 values (~ 50 K) and maximum lasing temperature (~ 380 K) have been achieved in state-of-the-art ICLs [34]. Clearly the subpar performance of the ICL under this study is not limited by fundamental physics and its strong temperature dependence of the lasing threshold current is not intrinsic to ICLs. Lack of carrier clamping in ICLs operating at higher temperature has been reported [35]. As the ICL under study does not lase beyond 248 K, the observed carrier clamping from our SVM measurements may only apply to low temperatures. It is worth noting that the SVM data also reveals substantial hole accumulation in the first AlSb hole well of the electron-injector section, which may induce considerable electron–hole nonradiative recombination, leading to another potential carrier leakage channel. It is unclear how big a role this leakage channel may play in the reduction of carrier lifetime, which merits further research effort.

4. Conclusion

In conclusion, a novel cryogenic-temperature scanning voltage microscopy technique has been applied to probing

the inner workings of an operating interband cascade laser – internal electric potential, internal electric field and internal charge-carrier density. The voltage-distribution profile across the eight cascade modules of the devices was measured at different device biases and temperatures at nanometer scales with high precision. The SVM results clearly reveal a nonuniform internal electric-field distribution in the active sections of the devices, confirming the spatial segregation of electrons and holes due to the unique type-II bandgap alignment in the device. The charge-carrier sheet density is derived from the SVM data, which is essentially clamped in the presence of stimulated emission at low temperatures. The temperature-dependent measurements indicate that the Auger recombination process may be a major carrier-relaxation mechanism at high temperatures, through which threshold current is significantly increased. The understanding of such a process and other potential leakage mechanisms would help to improve the device performance at high temperatures. Nevertheless, the demonstration of resolving dynamic charge-carrier density distribution in an operating optoelectronic laser device is unprecedented and could open the door to many future applications in probing the underlying mechanisms for many puzzling issues such as subpar performance and degradation in nanoelectronic devices, quantum devices and optoelectronic devices.

Supporting Information

Additional supporting information may be found in the online version of this article at the publisher's website.

Acknowledgments. The authors thank Y. Jiang, M. B. Johnson, J. C. Keay, T. D. Mishima, M. B. Santos, Z. Wasilewski, E. Dupont, M. Ferguson and A. Melvea for valuable discussions and technical assistance. We acknowledge financial support from the Natural Science and Engineering Research Council (NSERC) of Canada, the Canadian Foundation of Innovation (CFI), the CMC Microsystems, and the Ontario Research Fund (ORF). The laser work at the University of Oklahoma was supported in part by the National Science Foundation (ECCS-1002202), and by C-SPIN, the Oklahoma/Arkansas MRSEC (DMR-0520550).

Received: 26 June 2014, **Revised:** 8 October 2014,

Accepted: 19 January 2015

Published online: 17 February 2015

Key words: Interband cascade lasers, photonics, nanoprobe, charge carrier distribution, scanning voltage microscopy.

References

- [1] G. P. Agrawal and N. K. Dutta, Long Wavelength Semiconductor Lasers (Springer, New York, 1986).
- [2] P. Werle, F. Slemr, K. Maurer, R. Kormann, R. Mucke, and B. Janker, Opt. Lasers Eng. **37**, 101–114 (2002).
- [3] I. P. Kaminow, T. Li, and A. E. Willner, Optical Fiber Telecommunications VIA Components and Subsystems (Academic Press Wiley, 2013).

- [4] Y. Yao, A. J. Hoffman, and C. F. Gmachl, *Nature Photon.* **6**, 432–439 (2012).
- [5] G. Scalari, C. Walther, M. Fischer, R. Terazzi, H. Beere, D. Ritchie and J. Faist, *Laser Photon. Rev.* **3**, 45–66 (2009).
- [6] E. Murphy, *Nature Photon.* **4**, 287 (2010).
- [7] B. S. Williams, *Nature Photon.* **1**, 517–525 (2007).
- [8] S. Fatholoulumi, E. Dupont, C. W. I. Chan, Z. R. Wasilewski, S. R. Laframboise, D. Ban, A. Matyas, C. Jirauschek, Q. Hu, and H. C. Liu, *Opt. Exp.* **20**, 3866–3876 (2012).
- [9] L. V. Asryan and R. A. Suris, *Semicond. Sci. Technol.* **11**, 554–567 (1996).
- [10] R. S. Geels, S. W. Corzine, and L. A. Coldren, *IEEE J. Quantum Electron.* **27**, 1359–1367 (1991).
- [11] J. Faist, F. Capasso, D. L. Sivco, C. Sirtori, A. L. Hutchinson, and A. Y. Cho, *Science* **264**, 553–556 (1994).
- [12] R. Q. Yang, *Superlatt. Microstruct.* **17**, 77–82, (1995).
- [13] M. Kim, C. L. Canedy, W. W. Bewley, C. S. Kim, J. R. Lindle, J. Abell, I. Vurgaftman, and J. R. Meyer, *Appl. Phys. Lett.* **92**, 191110 (2008).
- [14] Rui Q. Yang, “Novel Concepts and Structures for Infrared Lasers”, Chap. 2, in *Long Wavelength Infrared Emitters Based on Quantum Wells and Superlattices*, edited by M. Helm (Gordon & Breach Pub., Singapore, 2000).
- [15] I. Vurgaftman, W. W. Bewley, C. L. Canedy, C. Soo Kim, M. Kim, J. R. Lindle, C. D. Merritt, J. Abell, and J. R. Meyer, *IEEE J. Sel. Top. Quantum Electron.* **17**, 1435–1444 (2011).
- [16] R. Q. Yang, L. Li, L. Zhao, Y. Jiang, Z. Tian, H. Ye, R. T. Hinkey, C. Niu, T. D. Mishima, M. B. Santos, J. C. Keay, M. B. Johnson, and K. Mansour, *Proc. SPIE* **8640**, 86400Q-1–10 (2013).
- [17] Y. Jiang, L. Li, Z. Tian, H. Ye, L. Zhao, R. Q. Yang, T. D. Mishima, M. B. Santos, M. B. Johnson, and K. Mansour, *J. Appl. Phys.* **115**, 113101–113101-9 (2014).
- [18] R. Weih, M. Kamp, and S. Hofling, *Appl. Phys. Lett.* **102**, 231123-1–4 (2013).
- [19] J. R. Meyer, C. A. Hoffman, F. J. Bartoli, and L. R. Ram-Mohan, *Appl. Phys. Lett.* **67**, 757–759 (1995).
- [20] R. Q. Yang, C. J. Hill, K. Mansour, Y. Qiu, A. Soibel, R. Muller, and P. Echtermach, *IEEE J. Sel. Top. Quantum Electron.* **13**, 1074–1078 (2007).
- [21] I. Vurgaftman, W. W. Bewley, C. L. Canedy, C. S. Kim, M. Kim, J. R. Lindle, C. D. Merritt, J. Abell, and J. R. Meyer, *Nature Commun.* **2**, 585-1–7 (2011).
- [22] W. W. Bewley, C. L. Canedy, C. S. Kim, M. Kim, J. R. Lindle, C. D. Merritt, J. Abell, and J. R. Meyer, *Opt. Exp.* **20**, 20894–20901 (2012).
- [23] W. W. Bewley, C. L. Canedy, C. S. Kim, M. Kim, J. R. Lindle, C. D. Merritt, J. Abell, and J. R. Meyer, *Opt. Exp.* **20**, 3235–3240 (2012).
- [24] E. Dupont, S. Fatholoulumi, and H. C. Liu, *Phys. Rev. B* **81**, 205311-1–18 (2010).
- [25] S. C. Lee and A. Wacker, *Phys. Rev. B* **66**, 245314-1–18 (2002).
- [26] H. Callebaut, S. Kumar, B. S. Williams, Q. Hu, and J. L. Reno, *Appl. Phys. Lett.* **83**, 207–209 (2003).
- [27] C. Jirauschek and P. Lugli, *J. Appl. Phys.* **105**, 123102-1–5 (2009).
- [28] D. Ban and E. H. Sargent, *IEEE J. Quantum Electron.* **36**, 1081–1088 (2000).
- [29] D. Ban, E. H. Sargent, St. J. Dixon-Warren, I. Calder, T. Grevatt, G. Knight, and J. K. White, *J. Vac. Sci. Technol. B* **20**, 2401–2407 (2002).
- [30] D. Ban, E. H. Sargent, K. Hinzer, St. J. Dixon-Warren, A. J. SpringThorpe, and J. K. White, *Appl. Phys. Lett.* **82**, 4166–4168 (2003).
- [31] D. Ban, E. H. Sargent, St. J. Dixon-Warren, K. Hinzer, I. Calder, A. J. SpringThorpe, and J. K. White, *IEEE J. Quantum Electron.* **40**, 651–655, (2004).
- [32] W. W. Bewley, J. R. Lindle, C. L. Canedy, M. Kim, C. S. Kim, D. C. Larrabee, I. Vurgaftman, and J. R. Meyer, *J. Appl. Phys.* **103**, 013114-1–4 (2008).
- [33] A. Soibel, K. Mansour, Y. Qiu, C. J. Hill, and R. Q. Yang, *J. Appl. Phys.* **101**, 093104-1–4 (2007).
- [34] I. Vurgaftman, W. W. Bewley, C. L. Canedy, C. S. Kim, M. Kim, C. D. Merritt, J. Abell, and J. R. Meyer, *IEEE J. Select. Top. Quantum Electron.* **19**, 1200210 (2013).
- [35] B. A. Ikyo, I. P. Marko, A. R. Adams, S. J. Sweeney, C. L. Canedy, I. Vurgaftman, C. S. Kim, M. Kim, W. W. Bewley, and J. R. Meyer, *Appl. Phys. Lett.* **99**, 021102 (2011).